



BrightnESS

Building a research infrastructure and synergies for highest scientific impact on ESS

H2020-INFRADEV-1-2015-1

Grant Agreement Number: 676548

brightness

Deliverable Report: [D4.10 Test for technology demonstrator]



1 Project Deliverable Information Sheet

BrightnESS Project	Project Ref. No. 676548	
	Project Title: BrightnESS - Building a research infrastructure and synergies for highest scientific impact on ESS	
	Project Website: brightness.se	
	Deliverable No.: D4.10	
	Deliverable Type: report	
	Dissemination Level: To EC project officer	Contractual Delivery Date: 30 July 2017
		Actual Delivery Date: 4 th September 2017
	EC Project Officer: Anna-Maria Johansson, Maria Vasile	

2 Document Control Sheet

Document	Title: Test for technology demonstrator	
	Version: V1	
	Available at: https://brightness.esss.se	
	Files: D4.10_Large-area-Detectors	
Authorship	Written by	Bruno Guérard
	Contributors	Jean-Claude Buffet, Victor Buridon, Jean-Francois Clergeau, Sylvain Cuccaro, Fabien Lafont, Julien Marchal, Christophe Mounier, Martin Platz, Patrick Van Esch, Anton Khaplanov, Richard Hall-Wilton
	Reviewed by	Roy Pennings
	Approved by	ESS BrightnESS Steering Board



3 List of Abbreviations

- FAC - First Active Cell
- FPGA – Field Programmable Gate Array
- ILL - Institute Laue Langevin
- ESS – European Spallation Source
- RAMSES - Rapid Measurement and Specialized Environment Spectrometer
- TOF – Time of Flight
- TOT – Time over Threshold
- PHS (PH) – Pulse Height Spectrum (Pulse Height)
- FEM (FE) – Finite Element Method (Finite Element)
- MG – Multi Grid

4 List of Figures

- Figure 1: Schematic view of the RAMSES detector
- Figure 2: Inside view of one module
- Figure 3: FE calculations of one module with 50-mbar over-pressure
- Figure 4: the automatic control system currently under mounting
- Figure 5: Drawing of the new grid developed for the RAMSES MultiGrid
- Figure 6: Evolution of the grid design
- Figure 7: Stability measurement.
- Figure 8: Counting curves and PH spectra
- Figure 9: stability measurement with a source
- Figure 10: stability measurement on a neutron beam line
- Figure 11: counting rate versus HV at different pressures from 50 mb to 1 bar
- Figure 12: typical signals measured
- Figure 13: PH spectrum measured on the anode
- Figure 14: Correlation analysis
- Figure 15: TOT Analysis
- Figure 16: Cathode TOT spectra
- Figure 17: crosstalk measurement
- Figure 18: photo of the MG12 prototype mounted on CT1
- Figure 19: Pulse Height spectra measured on Grid#5-7 at different positions of the beam.
- Figure 20: Variation of the multiplicities versus discrimination threshold
- Figure 21: Direct result of the localization algorithms
- Figure 22: Calculation of the RMS of the average position

Table of Contents

1	Project Deliverable Information Sheet	2
2	Document Control Sheet.....	2
3	List of Abbreviations.....	3
4	List of Figures	3
5	Executive Summary.....	4
6	Report on Implementation Process and Status of Deliverable.....	5



7	Technical Content	7
7.1	Concept implementation of the detector.....	7
7.2	RAMSES MultiGrid (RMG) design.....	9
7.3	Gas flushing.....	11
7.4	Stability measurement at low pressure	11
7.5	Stability measurement at atmospheric pressure	13
7.6	Stability measurement with the MG12.....	15
7.7	MG12 Measurements on CT1.....	15
7.8	Signal analysis with the MG12 at atmospheric pressure.....	16
7.9	Signal analysis with the MG12 filled with pressure from 1 bar to 50 mbar	18
7.10	Position measurements.....	20
8	Conclusion	24
9	Bibliography	25

5 Executive Summary

The organization of BrightnESS Work Package 4 task 4.3 relies on the interaction between the European Spallation Source ERIC (ESS) and the Institut Laue-Langevin (ILL) detector teams to make the best Multi-Grid technology [1-8] available for the ESS instruments at the first day of operation. Two approaches are considered in this task: on one side, ESS is focusing on the simulation, design, construction and characterization of a demonstrator detector containing detection elements, called grids, similar to the IN5 Grid developed previously in the CRISP project. This baseline, described in the BrightnESS D4.5 deliverable, ensures production feasibility and predictable operation of the detectors for the ESS instruments at Day-1. On the other side, the development carried out at ILL is mainly focused on the study of a new grid, called RAMSES Grid, with the aim of:

1. reducing the dead zones of the detector, and
2. improving the intrinsic detection efficiency.

ILL and ESS developed a 3 m long 8-columns prototype, called the IN5_Prototype, before the BrightnESS project. The walls used to reinforce the structure of the vessel limited its global efficiency. The weight of one module, 700 kg, a factor of around 2 higher than IN5, also represents a severe drawback for the integration into an instrument. Most of the Time-of-Flight (TOF) instruments of ESS are planned to operate in vacuum. The new approach studied in the BrightnESS project, is to reduce significantly the requirements on the mechanical strength on the detector vessel in order to reduce the need of reinforcement walls, by operating the detector at low gas pressure.

Compared to the IN5 Grid, the performance gain expected from the RAMSES Grid comes from a factor 3 larger dimension and from an increased ratio between convertor surface and grid volume. Due to the higher number of blades it contains, the RAMSES Grid is more delicate to fabricate than the IN5 Grid. Several design iterations have been necessary to reach a satisfying mounting procedure and the desired precision. The size of the RAMSES Grid imposes the use of large pressure vessels and a gas over-pressure inside the detector vessel, between 0 and 100 mbar, independent from the external pressure which ranges from 0 bar when the instrument Time-Of-Flight Chamber is under vacuum, to 1 bar when the TOF chamber is open for setting up the scientific experiment. By requiring an overpressure of 50 mbar max, it is



possible to further reduce the thickness of the detector entrance window to minimize the background noise coming from neutron scattering.

In addition to the mechanical advantage of reducing the gas pressure from 1 bar to 50 mbar, a significant benefit on the detector operation was also measured: first, the gamma background noise is significantly reduced, and second, the anode wire stability is improved thanks to the lower applied voltage. This pressure condition requires the development of a dedicated automatic gas control system, which will also provide a continuous flushing of the gas inside the detector vessel to remove molecules coming from outgassing of the internal parts; the proper flow rate must be defined to minimize gas consumption while providing stable operation. One disadvantage of low pressure operation is the higher flow rate required to maintain the outgassing molecules at an acceptable level; this disadvantage must be mitigated by the selection of the detector components to reduce outgassing.

In parallel to the development of the RAMSES design, different signal processing algorithms were developed to improve the precision of the position measurement. These algorithms are easily implementable on FPGA circuits and are independent of the detector design; they could be used on the ESS 'instrument suite on day-1' as a later upgrade if necessary. In summary, the work carried out in this deliverable is an important contribution to the possibilities for utilisation of the Multi Grid detector technology on ESS instruments as well as its application in instruments at other facilities. The design and testing performed both show how this design can be engineered, as well as how performance can be improved by advances in the design. As well as the advances detailed above, this deliverable includes two annexes with the engineering details relevant to specific aspects of the design, namely the implementation of a low pressure gas system and the mounting of larger dimensioned grids.

6 Report on Implementation Process and Status of Deliverable

RAMSES (Rapid Measurement and Specialized Environment Spectrometer) is the name of the instrument proposed in the "Endurance" modernization program of the ILL to replace the IN6 instrument. It is a time-focusing time-of-flight spectrometer designed for quasi-elastic and inelastic scattering. It will provide extended and continuous wavelength range from 6 Å down to 2.5 Å, extended coverage of scattering angles, and the highest possible flux at the sample position with a 1x1 cm² beam spot. Special emphasis is put on the incorporation of advanced sample environments including an option for beam compression. A gain of 20 in the 1x1 cm² beam spot with an energy resolution comparable to that of IN6 is expected. Dedicated optical elements for beam compression placed between the Fermi chopper and the sample can increase the flux in a 2 mm high spot a further factor two, depending on the wavelength. The expected flux is of the order of 10⁶ Hz on the sample. In order to fully benefit from the high flux on the sample, the detector of RAMSES must be as efficient as possible and its background must be less than 0.003 Hz in 2.5 x 2.5 cm² at 250 cm distance from the sample. More information about Endurance can be found at: <http://www.ill.eu/about/modernisation-programmes/endurance/the-endurance-projects-june-2013/>

At the time of writing this report, the RAMSES project is still in discussion and its implementation has not been decided, nor has the detector technique been selected. The name "RAMSES Multi-Grid detector" stands for the prototype being developed at the ILL with the following specifications:

- Pressure of the detection gas: 50 mbar
- Purification of the detection gas by continuous flushing



- TOF chamber under vacuum (option: a few mbar bellow 50 mbar)
- Radius of curvature: 2.4 m
- Angular range: 145° covered by 12 modules of 12° each mounted side by side
- Angular resolution: 0.375°
- Uniform response of the detection channels in one module
- Improved detection efficiency compared to the previous CRISP design
- Dead space equivalent to 1 pixel between 2 modules

The operation of the detector at low gas pressure and the rapid changes of pressure in the vacuum chamber will be managed automatically by a dedicated system. Its principle is described in the annex 1. The programming of the processor to control the different parts of the gas control system is planned for September 2017, and the full gas system will be operational at the beginning of 2018.

The prototype is now equipped with two types of grids: 3 columns of IN5 "old" grids on one side, and 1 column of the "new" RAMSES grids on the other side. Both types of grids fill the same volume inside the detector vessel. The prototype started to be operational at the time of writing this report; preliminary results with an Am-Be source show that the detection efficiency obtained with the new grid is improved by at least 20% compared to the old grids. This result needs confirmation with a test on a monochromatic beam line. This will be done in October 2017 after the long shutdown of the ILL reactor.

Measurements show that the average dead time measured at 200 mbar pressure of Ar-CO₂, after optimization of the shaping amplifier, is 320 ns. This is a factor of 10 better than what was measured during the CRISP project at atmospheric pressure and non optimized amplifiers. The result confirms the good counting rate performance obtained by ESS. Furthermore, there was no evidence of ageing after 15 hours of intense irradiation.

The detector efficiency is constant from 1 bar to 50 mbar, and the plateau ranges are very similar from 50 mbar to 200 mbar, which makes the detector non sensitive to small variations of pressure. This feature, combined with the low voltage operation, make the detector a robust solution which is not sensitive to mechanical defects. It will facilitate transfer to the industry for mass production.

Data acquired with the IN5 grids exposed to a collimated neutron beam have been analyzed with several localization algorithms. The results, which do not depend on the type of grid, show that some of these algorithms that are easily implementable on an FPGA circuit, greatly enhance the precision of the position measurement compared to the standard First Active Signal algorithm, used traditionally.

When a neutron produces a signal on one grid, the neighboring grid exhibit a signal with a height equal to 16% of the primary signal. This ratio is higher than expected when taking into account the calculated capacitive coupling between the grids. We identified the origin of this discrepancy as coming from a high entrance impedance of the amplifiers. Recent results with new amplifiers having lower entrance impedance show a cross-talk reduced to less than 3%. This correction can potentially greatly improve the localization precision in future measurements.

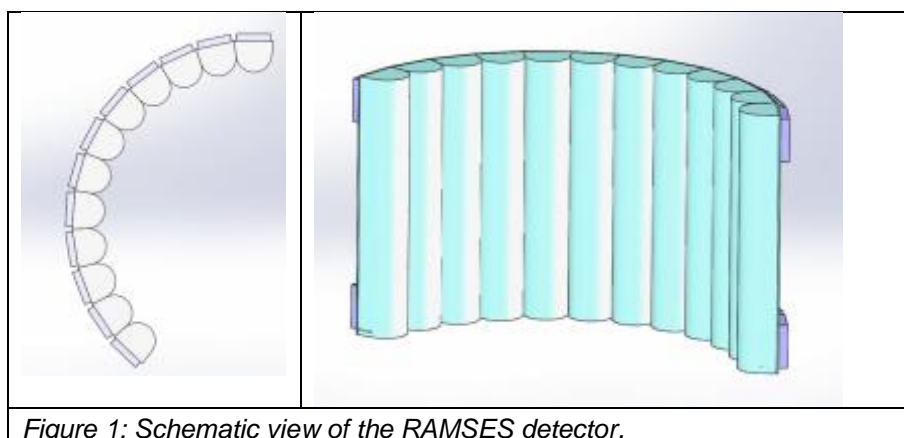
The prototype equipped with both the old and the new grids has been assembled and is now ready for a new test campaign on a neutron beam line. The goal will be to confirm the superiority of the new grid design in terms of detection efficiency and response uniformity. The next test campaign will also confirm the benefit of new localization algorithms; one of these algorithms will be implemented in the FPGA-based acquisition system for online processing. We

have validated the principle of a dedicated gas monitoring system for operation at 50 mbar, and for optimized flushing. The system is in fabrication and will be tested during 2018.

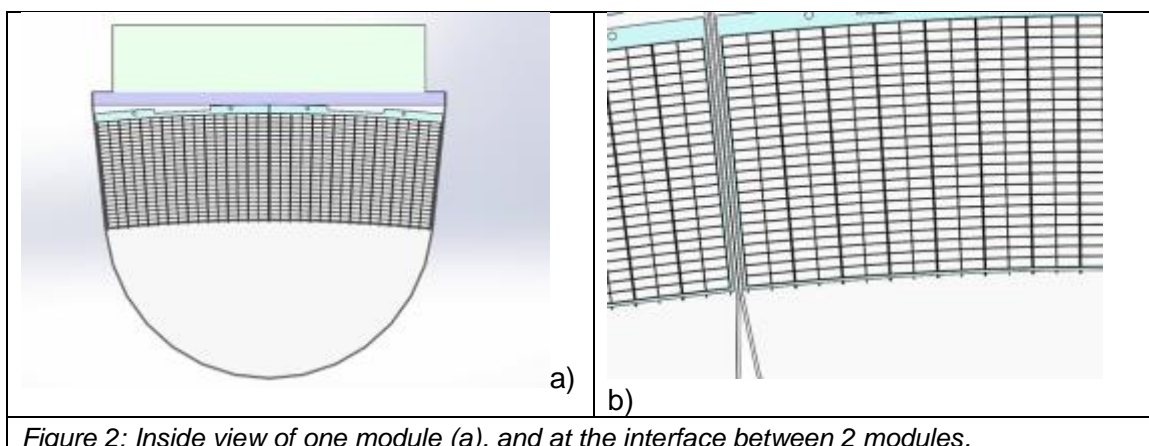
7 Technical Content

7.1 Concept implementation of the detector

Figure 1 shows the concept implementation of the detector as it might look like inside the TOF chamber of the future RAMSES instrument. In the actual version, the detector is made of 12 modules, 3 m high, mounted side by side, with a radius of 2.4 m to cover a 145° solid angle.



Each module contains 2 columns of grids with only a few mm dead-space between them (Figure 2). The dead space between the grids in two neighboring modules corresponds to only one channel (0.375°).



In order to minimize neutron scattering and neutron absorption due to interactions with the entrance window, a cylindrical shape is considered. According to Finite Element (FE)

calculations (Figure 3) a window of 2 mm of Aluminium would be enough for 50 mbar of over-pressure.

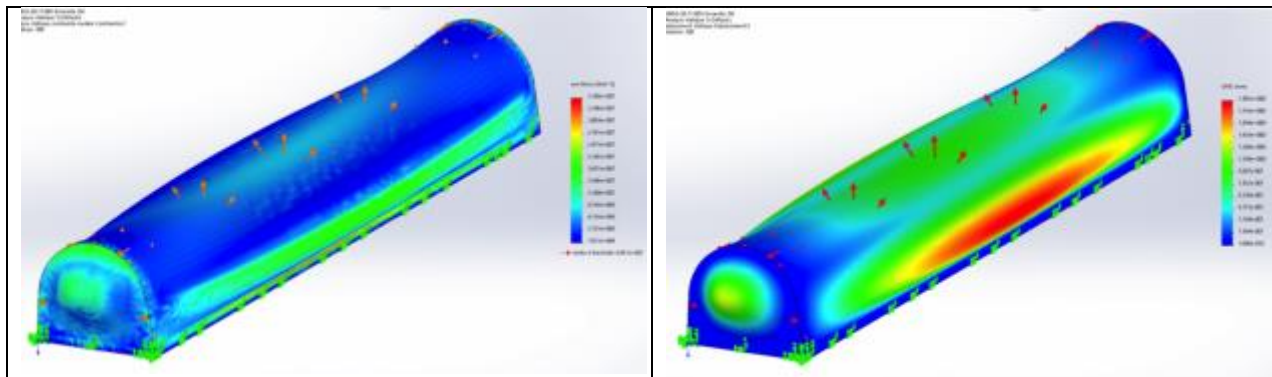


Figure 3: FE calculations of one module with 50-mbar over-pressure, showing strain (left) and deformation (right) of the detector vessel. The effective thickness "seen" by neutrons increases from 2 mm at the center of the module to around 6 mm for the first and last cells.

The integrity of the detector must be ensured even if the pressure inside the TOF chamber is changed without notice; the following items will ensure the safe operation of the detector (see also Annex 1 for details):

- automatic control of the gas pressure to keep the difference of pressure inside and outside the detector vessel below the limit imposed by mechanical constraints,
- automatic control of the power supplies: HV and LV must be shut down if the pressure inside the detector is changed.

A photo of the gas system during mounting is shown in Figure 4.

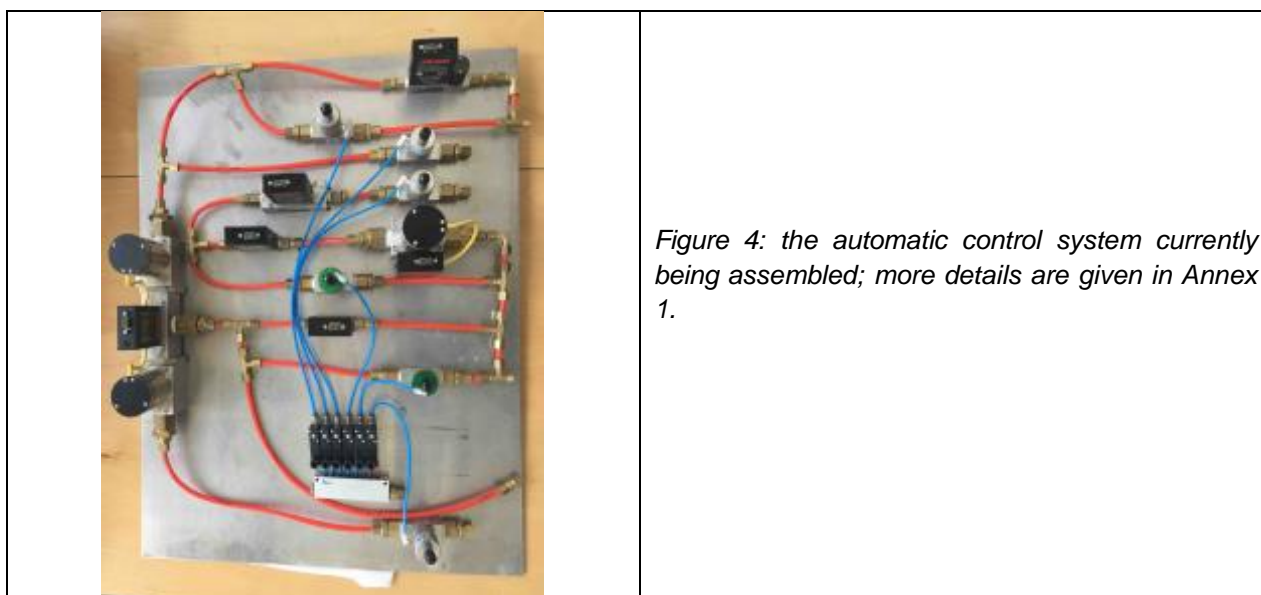


Figure 4: the automatic control system currently being assembled; more details are given in Annex 1.



7.2 RAMSES MultiGrid (RMG) design

Compared to the IN5 grid design, several important changes have been introduced in the RAMSES grid design:

- A significant gain in detection efficiency will be achieved from a number of B4C films in the Z direction (parallel to the beam) increased from 34 to 48, while keeping the total depth of the detector unchanged
- The radial blades (mounted along z) will be also coated with B4C, resulting in higher detection efficiency, and a reduced neutron scattering effect inside the detector
- The geometry of the grids has been adapted to the cylindrical shape of the instrument to minimize the dead volumes, and to improve the spatial uniformity
- The operation at low gas pressure will help reducing the interactions of gammas and to minimize the thickness of the detector window, hence the neutron absorption and neutron scattering
- Finally, the operation of the detector with a low pressure of the detection gas, combined with a proper choice of the amplifier shaping time, allows in principle reducing the dead time, hence to increase the counting rate capability.

The RAMSES grids are larger by a factor of 3 compared to the IN5 grids and the number of cells is multiplied by 5.65, which increases the complexity of their fabrication.

The surface of B4C per unit of solid angle is directly related to the detection efficiency.

If the radial blades (which are also coated with B4C) are not taken into account, RAMSES will increase this parameter by 50%. The gain becomes 100% if the radial blades are taken into account. Due to their orientation, approximately parallel to the trajectory of neutrons scattered by the sample, the radial blades contribute weakly to the detection efficiency ; ideally they should be coated with a thick B4C film to reduce the background noise by absorbing neutrons impinging the radial blades with a large incident angle

Figure 5 shows the drawing of the RAMSES grid and Figure 6 the evolution of the MultiGrid (MG) design.

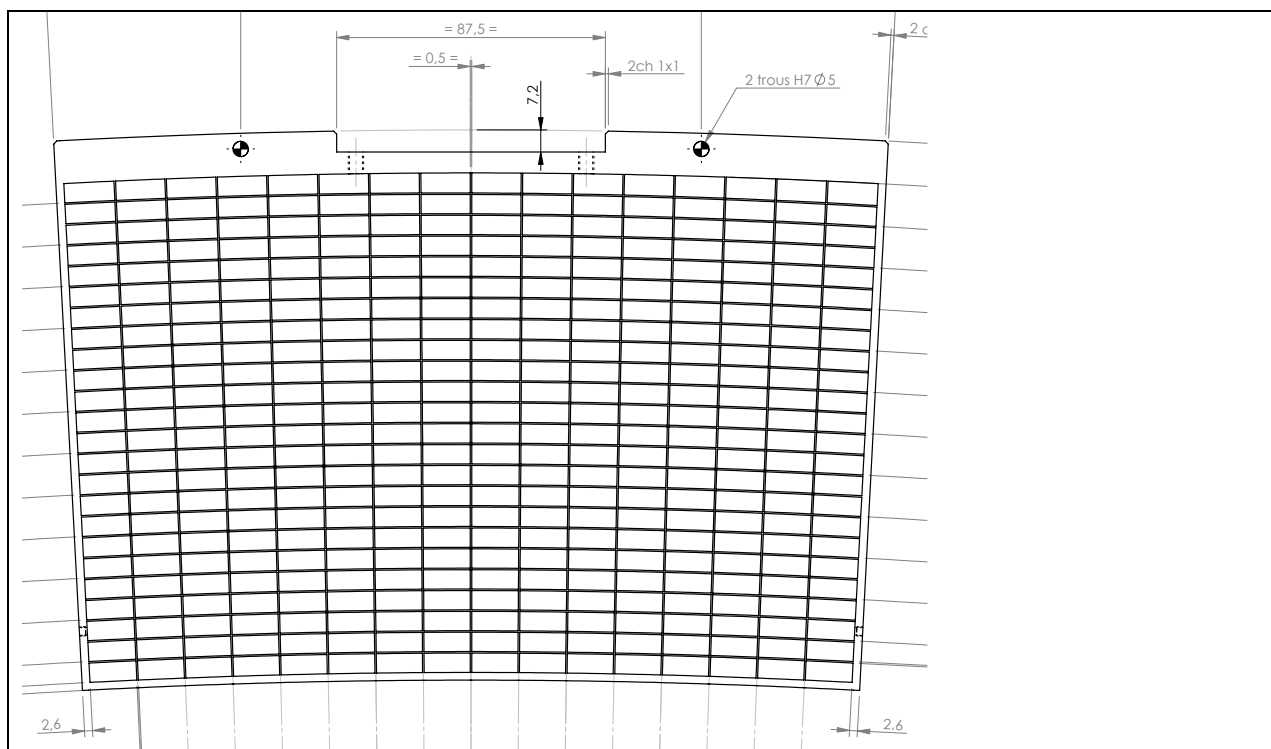


Figure 5: Drawing of the new grid developed for the RAMSES MultiGrid

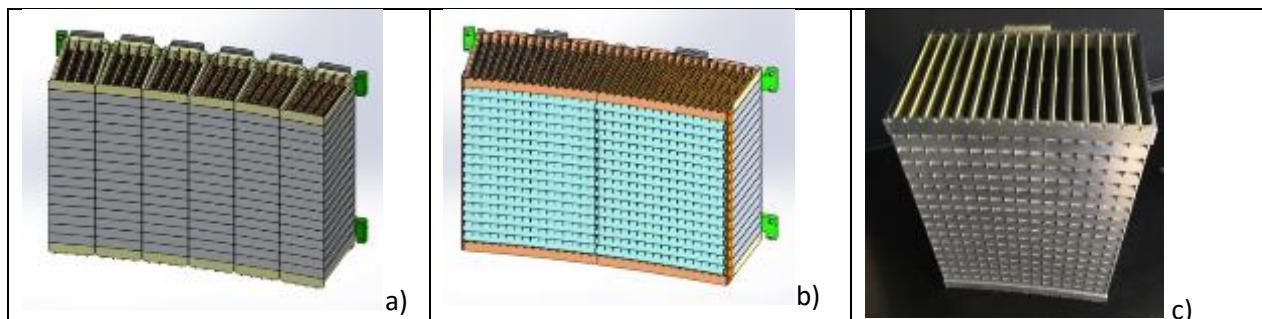


Figure 6: Evolution of the grid design

- a) The IN6 prototype studied during the CRISP project with 6 columns of 16 grids (new tests with an AmBe source will be described in this report).
- b) The RAMSES detector with 2 columns of 16 grids. The solid angle is the same as in a).
- c) one column of 16 RAMSES grids already mounted.

Each radial blade has been welded on both sides on the frame to compensate mechanical deformation in order to prevent short circuits between the grids, which are at only 0.5 mm distance from each other. With this design it is not necessary to machine the slits by wire spark erosion as was done for CRISP: the first and the last radial blades play the same role as the slits in the IN5 design. More details on the grid mounting are given in annex 2.



7.3 Gas flushing

Operating the detector in vacuum helps to prevent the introduction of air molecules inside the detector vessel. The downside are the mechanics able to support the pressure difference. Because of the priority given to a light mechanical structure to reduce neutron scattering and dead zones, our approach is to operate the detector at low gas over-pressure. Furthermore, the internal mechanics of the detector includes some organic materials, in particular FR4 PCBs, which are known to outgas impurities which may capture free electrons, affecting the gas amplification gain. Organic materials inside the detector should be avoided as much as possible, and low outgassing materials, like Polyimide (Kapton) for PCBs, should be given the preference. However, it will not be possible to avoid some outgassing. With no gas flow going through the detector, the response of the detector would degrade continuously until it might become unusable. That is why the detection gas will be continuously flushed inside the vessel to prevent contamination. In order to ensure the response stability, the balance between fresh gas coming inside the vessel and impurities going out, and the pressure of the detection gas, must be constant. It is hence important to use a precise pressure regulator and to flush pure gas continuously at an adequate gas flow rate. The gas regulation system is described in annex 1.

By using a permanent gas flushing at high flow rate, the signals will be at maximum height and stable, even in the case of a small variation of the flow rate. On the other hand, high flow rate is expensive in terms of gas consumption since we do not plan to use a closed loop system due to the difficulty to purify CO₂-based gas mixtures. If the gas flow is too low, the detector might be exposed to electron attachment due to electro-negative impurities and its performance (detection efficiency and gamma discrimination) might degrade. Furthermore, the amplification gain might decrease locally in the exposed regions due to a permanent ageing effect. Indeed, the optimum flow rate provides the best compromise between gas consumption and detector stability and performance. Determining the maximum level of impurities compatible with long-term operation is a multi-parametric problem requiring long irradiation measurements. Until an answer can be given to this question, a conservative approach should be adopted, and low outgassing materials should be given strong preference in the fabrication of the detector. As a preliminary approach, we define arbitrarily the proper gas flow as the one, which allows reaching 90% of the counting obtained at high flow rate.

7.4 Stability measurement at low pressure

An important parameter to consider is the purification of the gas: what is the value of gas flow required to maintain adequate purity for detector stability? In order to address this question, the counting rate and the amplification gain of the prototype have been monitored during long periods of time at different flow rates. For this test, the detector was filled with 60 mbar and mounted in a vacuum chamber filled with 50 mbar of air in order to cool down the electronics through convection.

Measurements were performed at HV: 480V, with an Am-Be source (100 mCu). The detector was first pumped out for 2 hours in the vacuum chamber before filling to 60 mbar. We then filled the vacuum chamber with 50 mbar of air. The first test was carried out with 10-



mbar over-pressure. In these conditions, we observe a rapid decrease of the counting in function of time: a factor of 3 in 20 hours (Figure 7). This behavior is attributed to the rapid gas contamination, which induces a gain reduction. Then the pressure of the detector was increased from 60 to 70 mbar during 30 minutes and the flow increased by a factor of 2, and then reduced to previous conditions. The counting rate increased immediately after the pressure change, indicating that the increase of flow rate was efficient in reducing the effect of impurities. During the 2 hours after the pressure was set back at 60 mbar, the slope of the counting curve was the same as in the preceding period.

We then increased the flow rate during 90 minutes to purge the detector, until counting rate reached saturation. Then the valve was closed for around 2 hours and opened again at a lower flow rate. The detector was stable at around 90% max counting.

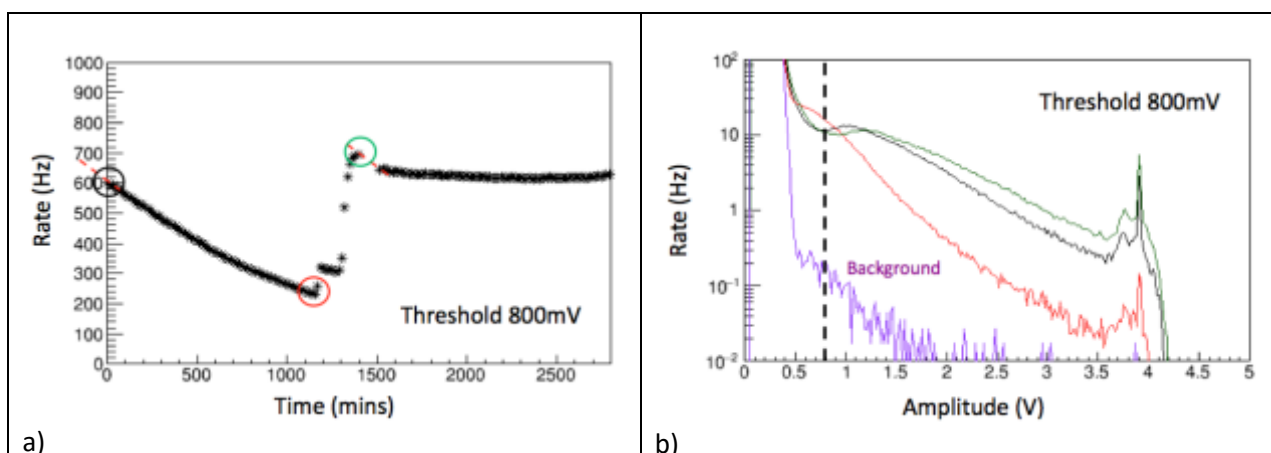


Figure 7:
 a) Stability measurement. During the first 20 hours, the flow rate was 0.75mL/min and pressure 60 mbar; it was then increased to 70 mbar during 30 minutes and set back at 60 mbar. Finally the vessel was purged at a higher flow rate, to reach stable operation.
 b) PH spectra measured at different times of the stability measurement (colors of spectra correspond to circle of same color).

The degradation is attributed to the large PCB mounted inside the vessel.

During the detector purge, the pressure inside the detector was reduced from 60 to 55 mbar in 1 minute. By using the following formula

$$P(t) = \Delta P * \text{Exp}(-\alpha.t) \quad , \text{ with } t \text{ in minutes, and } \Delta P = 60 \text{ mbar}$$

We obtain $\alpha = 0.087$

Hence the gas flow rate applied during the detector purge at 60 mbar is estimated to 130 mbar.litre/min, and to 50 mbar.litre/min after the purge. Around 20 bar.litre of gas have been used for the purge without taking into account the fraction of detection gas already in the detector when the purge was started. When the detector is operated in vacuum, vacuum pumping the detector is of course more efficient than flushing to evacuate impurities. This was



not implemented, however, in the present setup due to the 50 mbar of air in the vacuum chamber required for cooling down the electronics.

7.5 Stability measurement at atmospheric pressure

The prototype must be filled with 1 bar of detection gas for testing on the ILL CT1 beam line; before that, several volumes of detector have to be flushed to purge it.

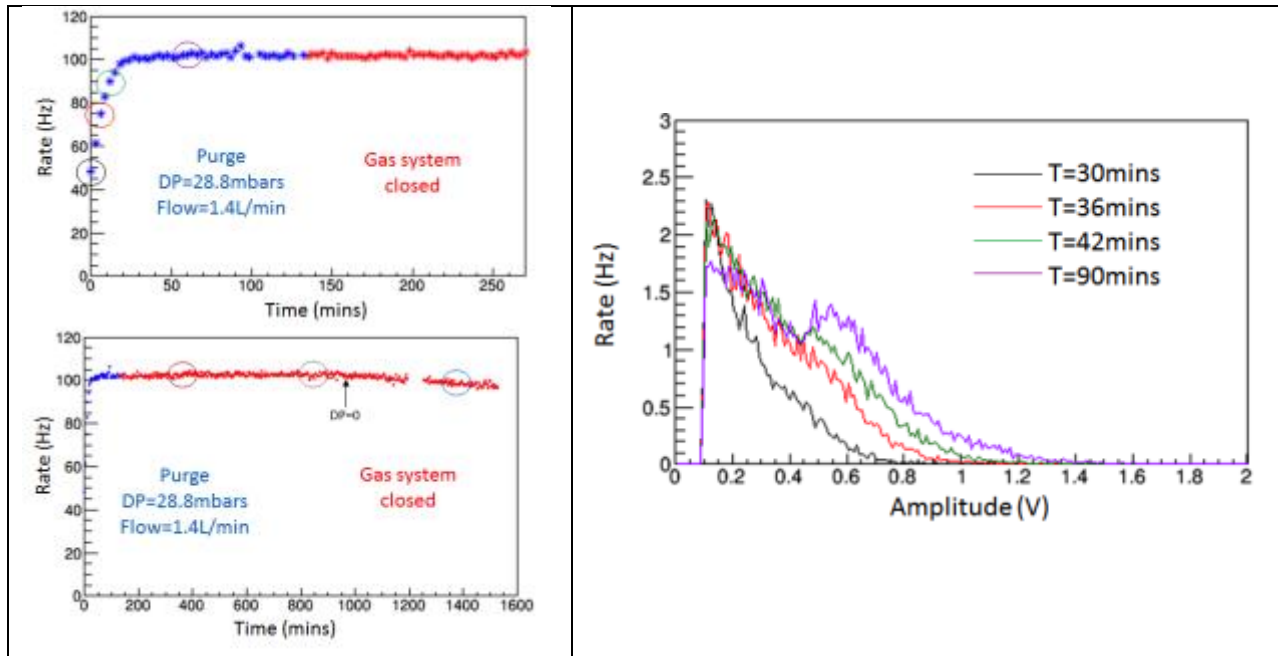


Figure 8: Counting curves and PH spectra (HV=850 V) measured at different time.

In order to know how many volumes of gas must be flushed before starting the measurements, we performed a counting rate measurement at a flow rate of 1.4 bar.l/min (measured with the pressure variation on the bottle gauge). Measurement shows that stable regime (90% max counting) is obtained after 42 minutes, corresponding to 2.35 times the detector volume (Figure 8). Simple calculations allow quantifying the proportion of detection gas after flushing a certain volume of gas.

Let's call V_{tot} the volume of the detector, $V_{gas}(t)$ the volume of detection gas in the detector at time t , ϕ the flow of gas entering the detector, and dV_{ar} the volume of detection gas entering the detector between t and $t + dt$

We have $dV_{ar} = \phi \cdot dt$

At any time we can write:

$$V_{gas}(t+dt) = V_{gas}(t) + dV_{ar} (1 - V_{gas}(t) / V_{tot}) = V_{gas}(t) + \phi \cdot dt \cdot (1 - V_{gas}(t) / V_{tot})$$



It follows:

$$V'_{\text{gas}}(t) + (\phi / V_{\text{tot}}) * V_{\text{gas}}(t) = \phi$$

The solution is:

$$V_{\text{gas}}(t) = V_{\text{tot}} (1 - \text{Exp}(- \phi . t / V_{\text{tot}}))$$

The fraction of gas in the detector $V_{\text{gas}}(t) / V_{\text{tot}}$ after passing 2.35 times the volume of the detector is equal to $1 - \text{Exp}(- \phi . t / V_{\text{tot}}) = 90.5\%$

Surprisingly, the high fraction of air molecules inside the detector, around 10%, is not detrimental to its operation when operated at 1 bar. We continued the purge during 2 hours even without noticing any change of the counting rate. After that, the counting rate remained stable during 15 hours, and then started to decrease when the pressures inside and outside the detector were equilibrated. Figure 9 shows the counting curve at 1 bar for a flow rate of 2 mb.l/min while the detector was maintained at an overpressure of 6 mb relative to the atmospheric pressure. Variation of +-1% can be attributed to variations of the atmospheric pressure.

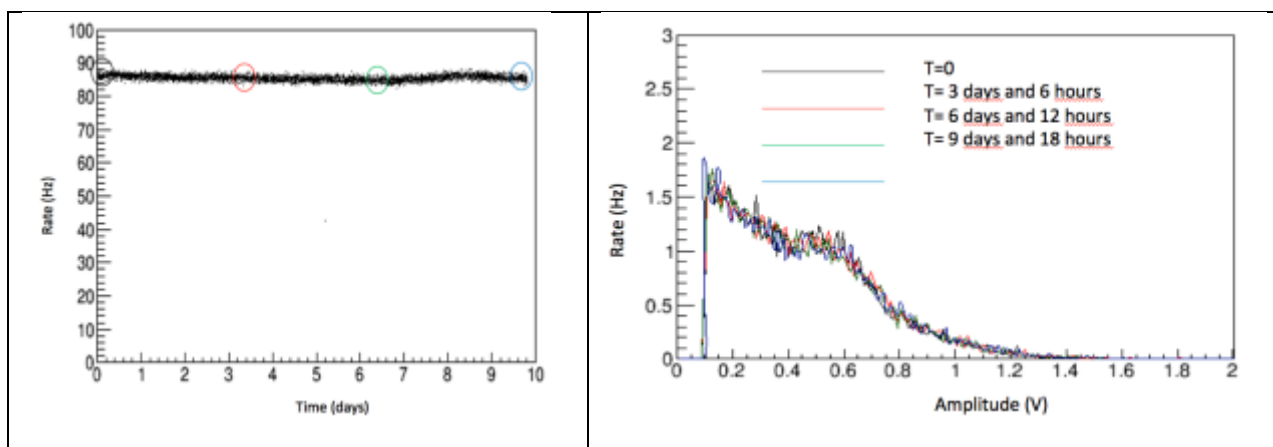


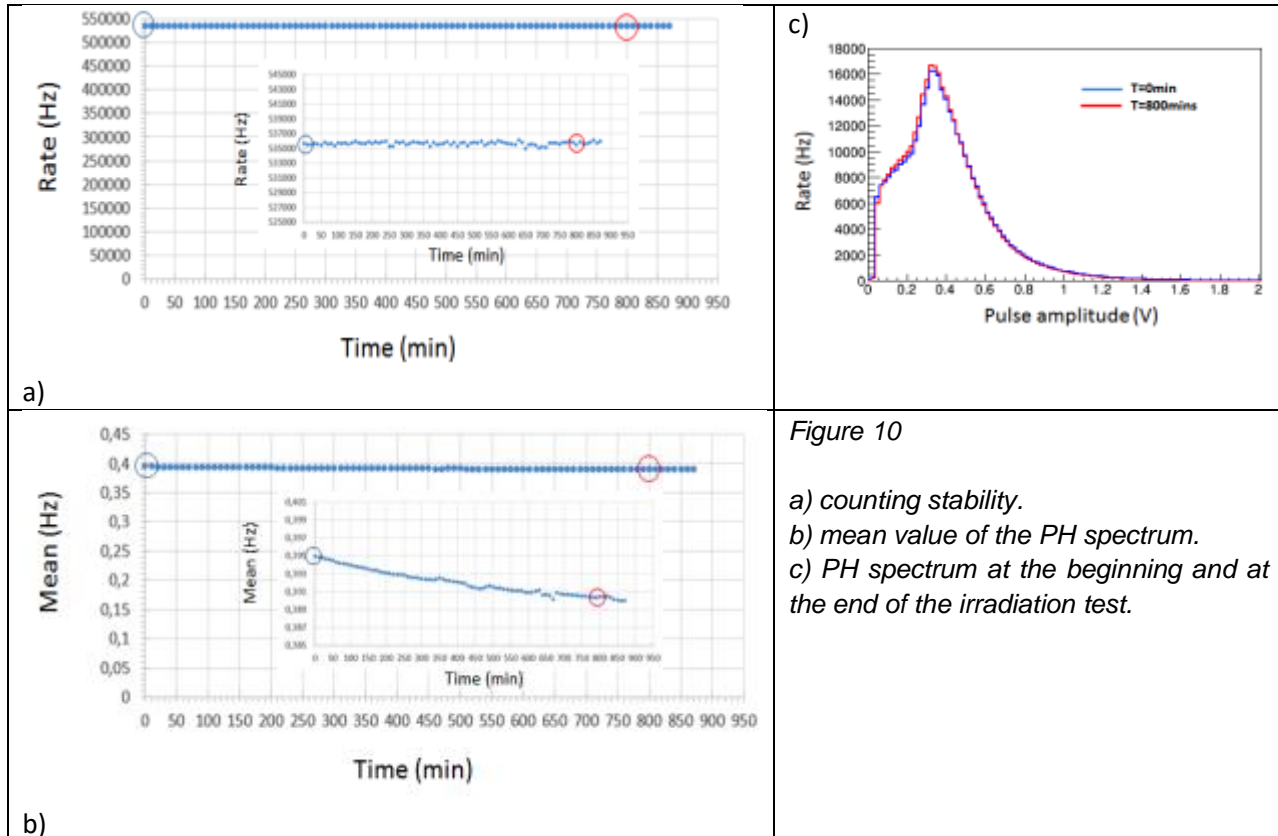
Figure 9
Stability measurement with the RAMSES proto at 1 bar at 2 mb.L/min.

This flow rate of 2 mb.L/min provides stable operation at maximum counting. The optimal flow could probably be reduced to optimise gas consumption. This should be compared with the much higher flow (50 mb.L/min) required at 50 mbar internal pressure to reach the minimum point of stability (90% efficiency). Operating the detector at 50 mbar requires at least 25 times more gas flow (in mbar.L/min) compared to 1 bar to reach stable operation. This is consistent with the fact that the outgassing rate does not depend on the gas pressure inside the vessel, hence the ratio between impurities and detection gas is similar for the 2 conditions.



7.6 Stability measurement with the MG12

The MG12 prototype is another detector containing only one column of grid, adapted for vacuum or gas pressure up to 10 bars. The detector was pumped out for 6 hours before being filled with 50 mbar of Ar-CO₂ (90:10). The stability curve measured at Van=520 V on CT1 neutron beam line is shown in figure 10. The counting rate and the PH spectrum were recorded during 15 hours of continuous irradiation on the CT1.



Despite this harsh irradiation test - the total number of neutrons detected being $3 \cdot 10^{10}$ - there wasn't any noticeable variation of the counting, and the average pulse amplitude decreased by only 2%. This measurement confirmed that the MG12 detector can be tested during several days without purifying the gas.

7.7 MG12 Measurements on CT1

The MG12 equipped with the XY-coincidence acquisition system was tested at different pressures from 50 mbar to 1 bar, and the resulting "counting versus HV" curves are shown in figure 11. Plateaus correspond to the full efficiency of the detector, which is 47%, measured at the centre of a grid with no border effect.

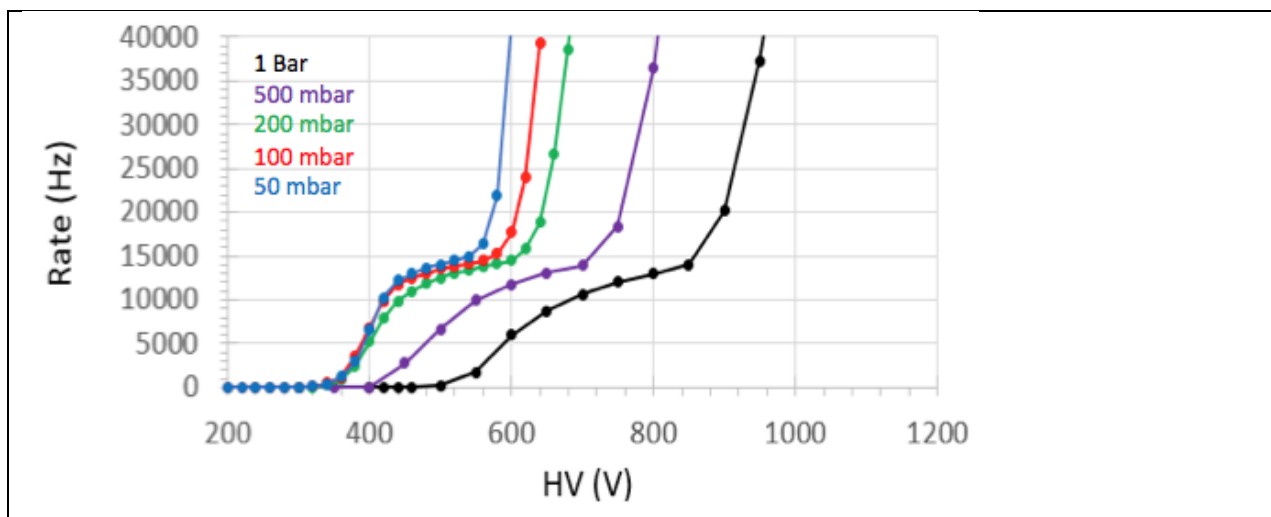


Figure 11
Counting rate versus HV measured with the MG12 at different pressures from 50 mb to 1 bar.

Counting plateaus start at 350 V for pressures between 50 mbar and 200 mbar; they start at higher values for 0.5 b and 1 bar. Compared to the curve at 50 mbar, the gamma rise is shifted to higher voltage, by 50 V for the curve at 100 mbar, and by 100 V for the curve at 200 mbar. The counting rate between 360 V and 520 V is almost the same for 50 mbar and for 100 mbar. In the absence of other effects, the counting rate depends only on the probability for a signal of charge $Q_{tot} = G * Q_{prim}$ to be higher than the discrimination threshold. It means that Q_{tot} has similar values for 50 mbar and 100 mbar between 360 V and 520 V. Even if we take into account the energy loss in the B4C film, the particles emitted in the gas (Lithium or alpha) have a range of several cm in the gas (3 cm at 200 mbar, 6 cm at 100 mbar, and 12 cm at 50 mbar for alphas; these ranges are a factor of 3 lower for the Lithium). Hence, only a small fraction of the energy is deposited in the gas. In a first approximation we can consider that the primary charge Q_{prim} realised in the gas at 100 mbar is 2 times higher in average compared to 50 mbar. It follows that the amplification gain around 400 V is 2 times lower for 100 mbar than for 50 mbar. The good match between the counting curves at 50 mbar and 100 mbar makes the detector non-sensitive to small variations of pressure when operated in this pressure range. It confirms the very good stability measured with the MG12 in the previous section.

7.8 Signal analysis with the MG12 at atmospheric pressure

The anode wires were connected together and read out with a charge amplifier with an integration time constant of 1 μ s and a gain of 4V/pC. This amplifier was originally used during the CRISP project. The cathode grids were connected together and read-out with a charge amplifier with an integration time constant of 80 ns and a gain of 28V/pC. Anode and cathode signals were recorded with an Acqiris system triggered with the anode signal and then analysed off-line. The analysis of these signals allowed us to compare the operation of the detector in different conditions (pressure, voltage).



The detector was pumped out for 6 hours and then filled with the detection gas at 1 bar. It was tested first at 1 bar and then at lower pressures down to 50 mbar by using a pump to reduce the pressure. Some typical events measured at 1 bar (HV=815 V) are shown in Figure 12

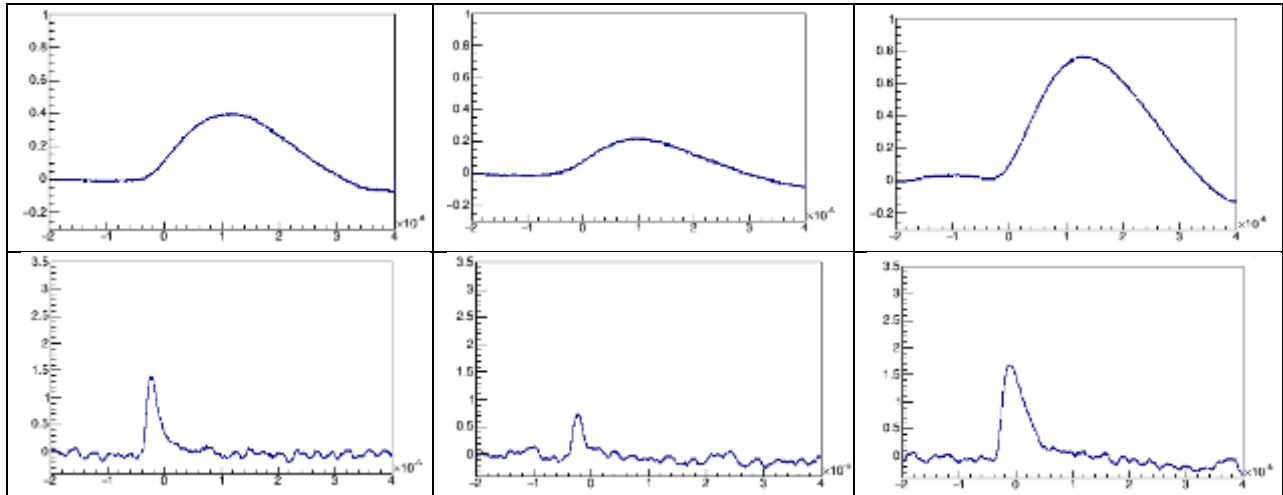


Figure 12
 Typical signals measured on the anode with the slow amplifier (first line), and corresponding signals measured on the cathode with a fast amplifier (second line). The signal on the cathode is noisy due to the large capacitance of the 12 grids connected together.

The PH spectrum measured on the anode (figure 13) shows that the events selected by the trigger are only neutrons, and that there is no selectivity of the events by energy: all neutrons interacting in the detector are detected.

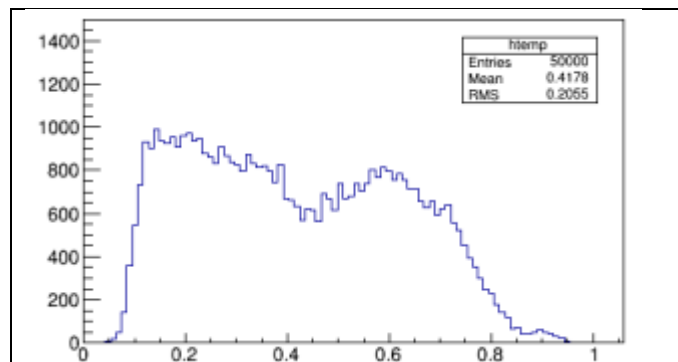


Figure 13
 PH spectrum measured on the anode for 50.000 events. This spectrum shows the typical double peak of a MultiGrid detector.

The fast shaping time of the cathode amplifier induced some ballistic deficit of the signals, which is illustrated by the PH spectrum shown in Figure 14 a). By summing numerically the signals, this ballistic deficit can be corrected as shown in 14 b). The effect of this correction can also be illustrated by comparing the "anode versus cathode signal height" plot (Figure 14 c), and the



"anode versus cathode numerical integral" plot (Figure 14 d): we see a much better correlation between anode and cathode signals with the numerical integral.

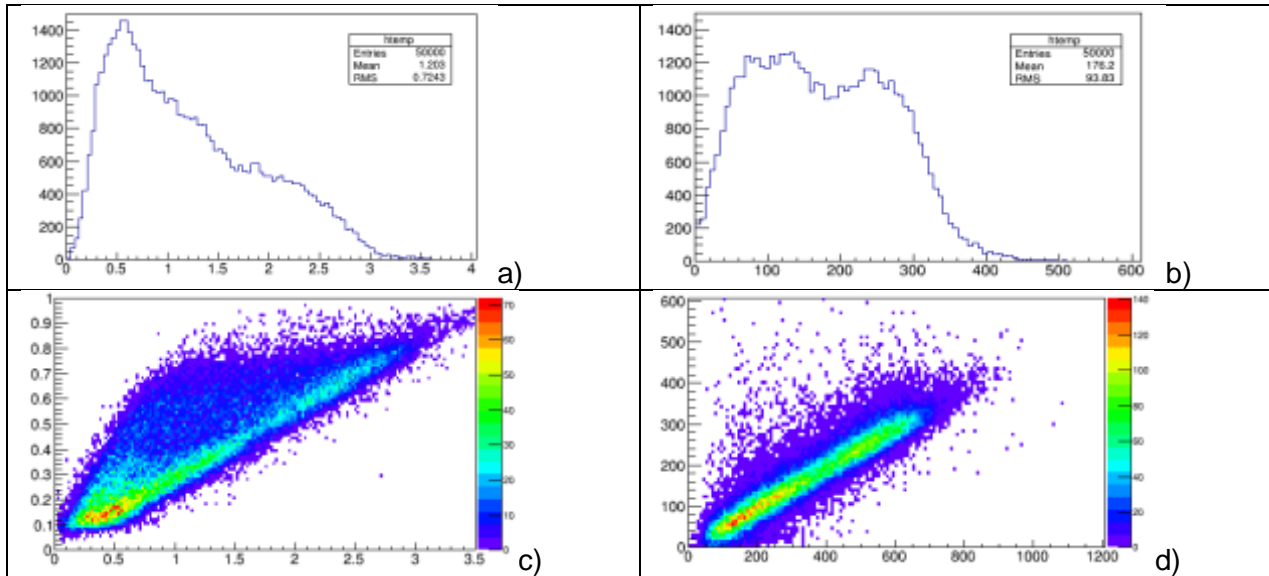


Figure 14
 PH spectrum on the cathode (a) and numerical integration of the cathode signal (b).
 Correlation between signal heights (c), and between numerical integrals (d)

7.9 Signal analysis with the MG12 filled with pressure from 1 bar to 50 mbar

Data was processed off-line to count the number of events with cathode signal height above the threshold. This analysis has been done for threshold values varying from 100 mV to 3 V; the result is shown in figure 15 a).

It should be stressed that voltage values were chosen arbitrarily in the plateau region of each counting curve. The results of figure 15 a) might change significantly for other voltage values. In order to avoid bias of the results, Time over Threshold (TOT) values should not be compared at fixed threshold, but at equal cathode detection efficiency. The curve Mean (TOT) versus cathode efficiency is shown in figure 15 b).

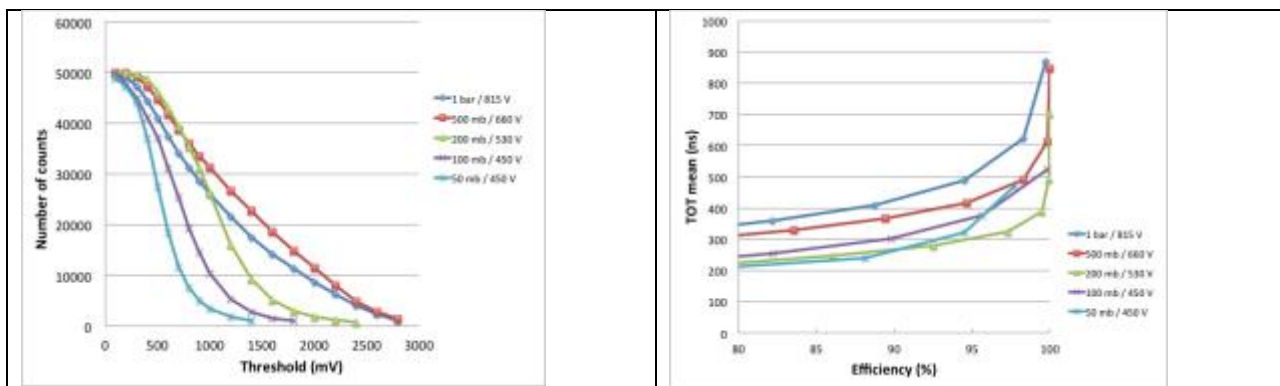




Figure 15: Analysis of Acqiris data
 left: Num. of counts versus discrimination threshold applied on the cathode.
 right: Mean value of TOT versus cathode efficiency = 100 * (Num. of counts / 50.000).

For 98% efficiency, we observed a reduction of $\langle \text{TOT} \rangle$ from 1 bar (620 ns) to 200 mb (320 ns) due to the increasing reduced Electric Field E/P (Figure 16), and then it slightly increased from 200 mb to 50 mb (470 ns). From this experimental result we believe that 200 mb is close to the optimal pressure in terms of the dead time and values between 200 mbar and 50 mb are all better than at 1 bar.

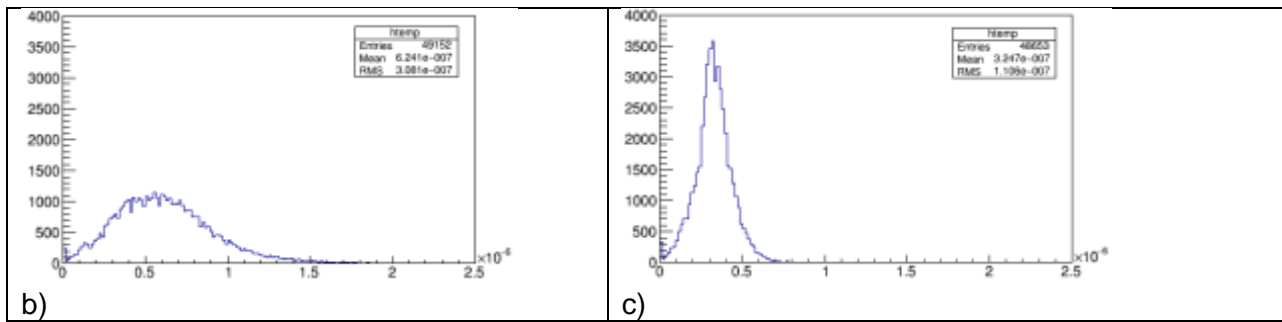


Figure 16: Cathode TOT spectra at 98% detection efficiency at 1 bar (b) and 200 mbar (c).

Operating the detector at low pressure provides a factor of 2 reduction in the time development of the avalanche signals. By taking into account (1) the factor 4 already achieved with an optimization of the signal processing, (2) the reduced size of the tube section, (3) the higher number of tubes and (4) further possible optimization, we are confident that the dead-time can be reduced by a factor of at least 10 for RAMSES compared to CRISP and that the counting rate capability can be increased by the same factor.

Due to the capacitive coupling between the grids, some crosstalk might occur between the channels with some possible degradation of the localization. Figure 17 shows the correlation spectrum between the signals measured on 3 neighboring grids. By irradiating the central grid and triggering on the corresponding channel, we measured for each event a crosstalk signal corresponding to 16% of the direct signal.

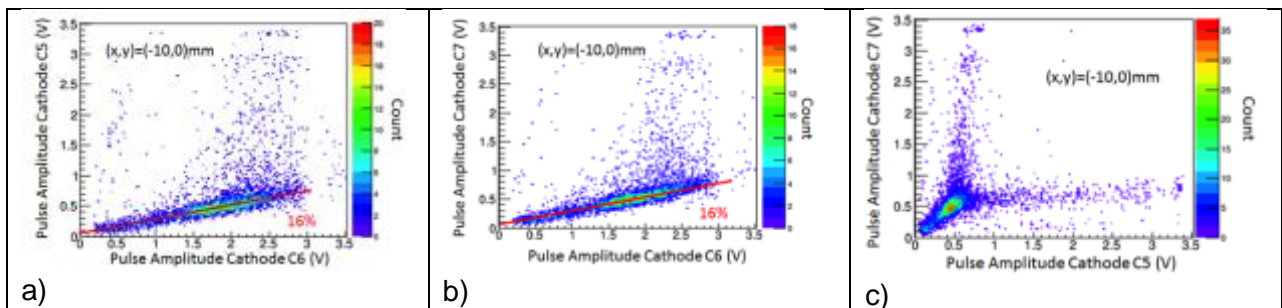


Figure 17
 Crosstalk measurement at 50 mbar (450 V) with MG12. Grid C6 is exposed to the neutron beam and is used as the trigger signal. A constant fraction (16%) of the C6 signal is measured on the 2 neighbouring grids C5 and C7.

7.10 Position measurements

The MG12 detector was mounted on the translation table of CT1 in front of the optical bench supporting the collimation system (Figure 18). A beam aperture of 2 mm x 2 mm allowed us to study the detector response locally by moving it vertically along z, and horizontally along x.

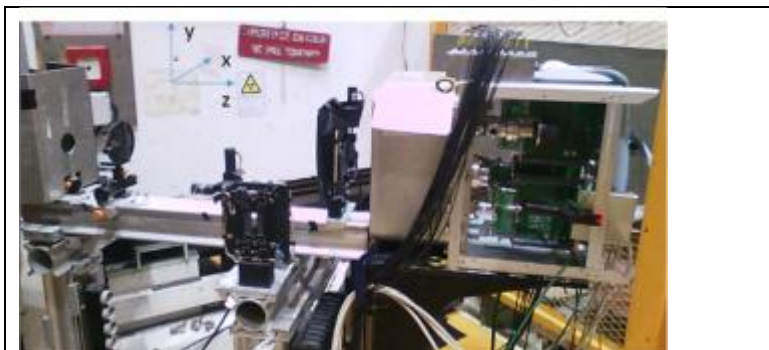


Figure 18
The MG12 prototype mounted on the monochromatic neutron beam (Wavelength: 2.5 Å) of CT1. A spot of 2 mm x 2 mm is defined by the collimation system.

Signal tracks were measured with a digital oscilloscope system (Acqiris) to analyse different localization algorithms in order to determine which one could be implemented without additional complexity of the front-end electronics. The First Channel N that generates a signal above the threshold V_{Th} is called the First Active Channel; it determines the 3-channel cluster (N-1, N, N+1), and its discrimination time $T(N)$ determines the time window for signal analysis. In the COG (Center Of Gravity) algorithm, the position of the neutron is given by the COG of the 3 channels, pondered by the charge measured on each channel. The charge is given by the numerical integral of the tracks during the integration time. The COG algorithm can't be implemented on all versions of the front-end electronics of the detector, as it would require the use of ADCs; it is therefore used for comparison with the other algorithms. In the First Active Cell (FAC) localization algorithm, the position of the neutron is simply measured as channel N. The idea with the LR (Left Right) algorithms is to compare the signals on channels N-1 and N+1 to improve the position measurement. 2 parameters are used to compare the signals: T (discrimination Time) in the LR_T algorithm, and TOT in the LR_TOT algorithm.

As for the FAC algorithm, the channel N corresponding to the first active signal is the one where the neutron is going to be located, but the channel N is divided in 2 sub-Channels N+ and N-. The position, N+ or N- is given according to the comparison between the T or TOT signals.

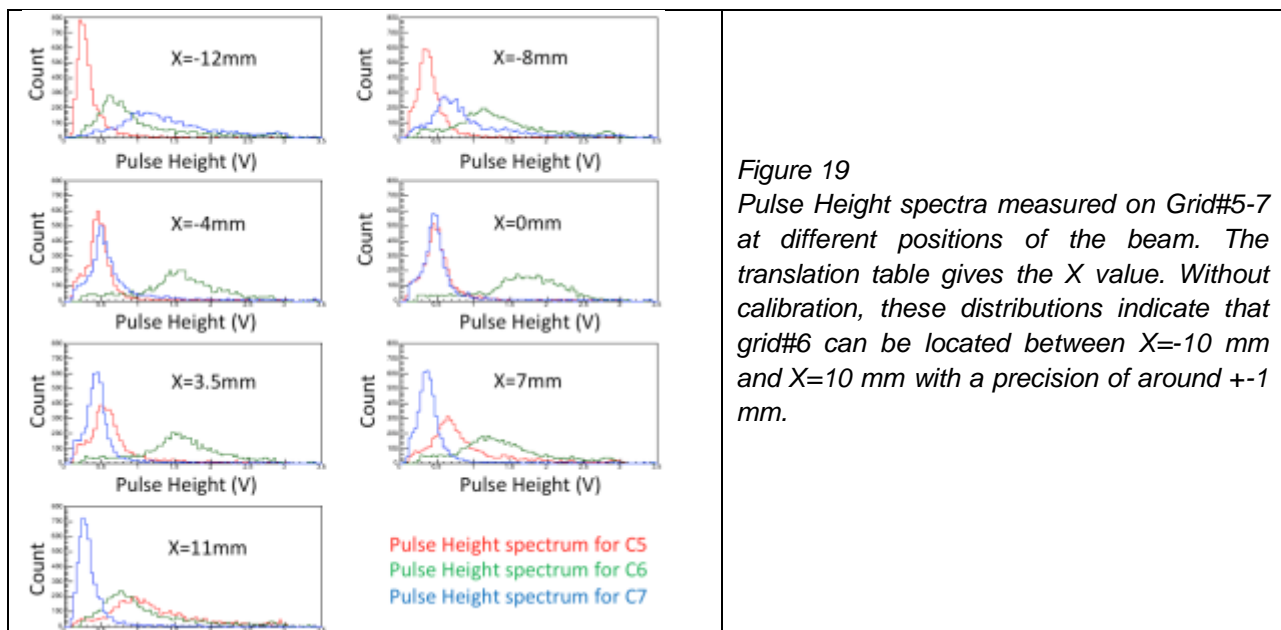
A summary of the different algorithms used for this analysis is given in the following table:

Algorithm	Variable	Principle	Remark
FAC	Discrimination Time $T(N)$	N with minimum $T(N)$	standard method
COG	numerical integral $I(N)$	COG of channel positions pondered by $I(N)$	for comparison only (requires ADCs)
LR_T	$T(N)$	N with minimum $T(N)$ is divided in 2 sub-	very simple to



		channels N_+ and N_- The neutron is localized in channel N_+ if $T(N+1) < T(N-1)$, and N_- in the other case	implement
LR_TOT	Time Over Threshold	The neutron is localized in channel N_+ if $TOT(N+1) > TOT(N-1)$, and N_- in the other case.	relatively simple to implement, but longer dead time compared to LR_T

Figure 19 below shows the pulse height spectra for beam positions from $X=-12$ mm to $X=11$ mm. Events are recorded for signals on Grid#6 > 250 mV. Digitized signals are recorded for Grid#5-7:



The multiplicity of the events is an important parameter for the LR algorithms. Its dependence with the discrimination threshold is illustrated in Figure 20. For $V_{th} = 0.5$ V, a majority of events has a multiplicity >1.

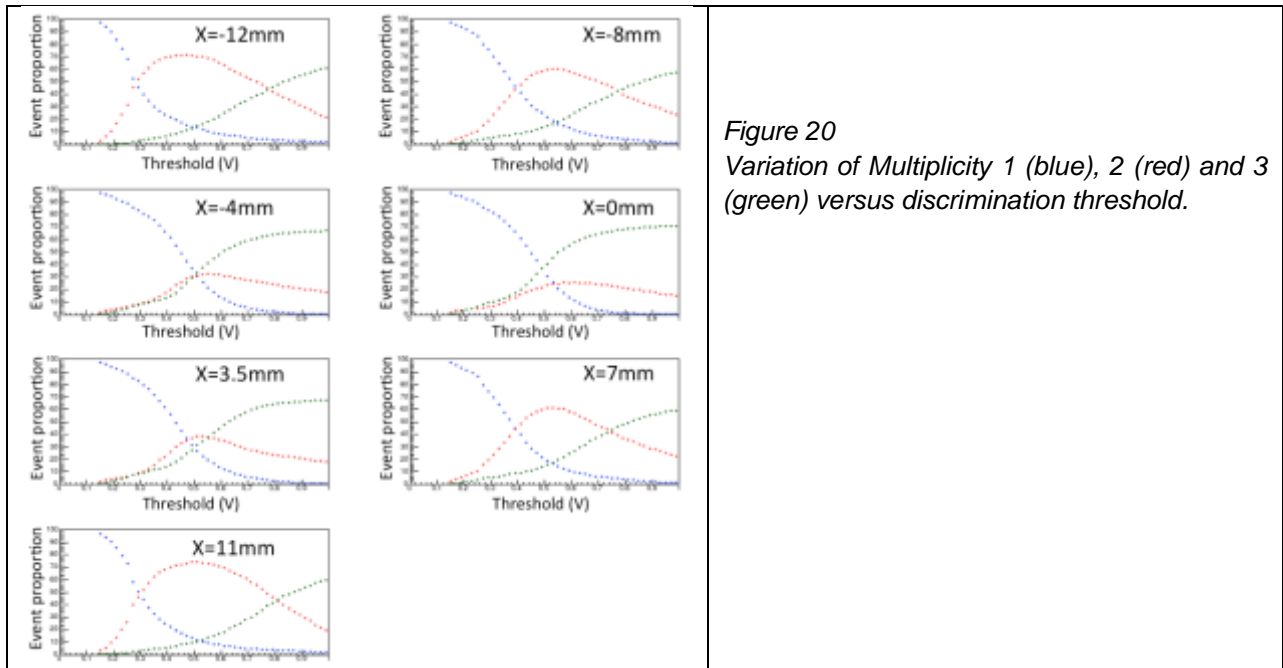


Figure 20
Variation of Multiplicity 1 (blue), 2 (red) and 3 (green) versus discrimination threshold.

Figure 21 below shows the direct result of the different localization algorithms:

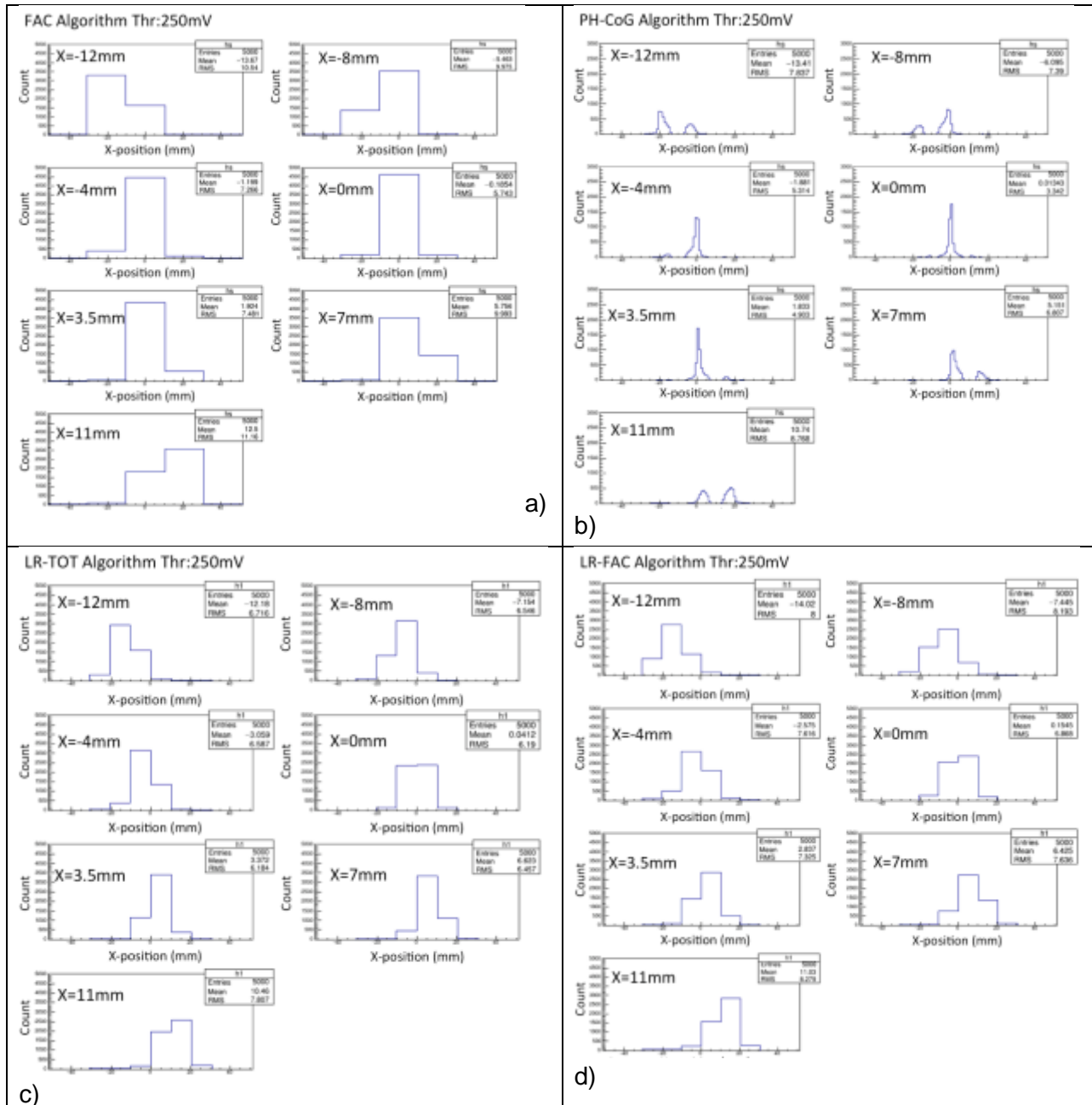


Figure 21
 Direct result of the different localization algorithms: a) FAC (First Active Channel), b) PH-COG (Pulse Height Center of Gravity), c) LR-TOT (Left-Right Time-Over-Threshold), d) LR-FAC (Left-Right First Active Channel).

In order to compare the results of these algorithms, the RMS of the average position measured in each run relative to the ideal position curve (linearity 1 and position offset allowing to minimize the RMS). The result is given in Figure 22. We see that the LR-TOT allows to improve by a factor 3 the precision of the average position compared to that obtained with the standard FAC method.

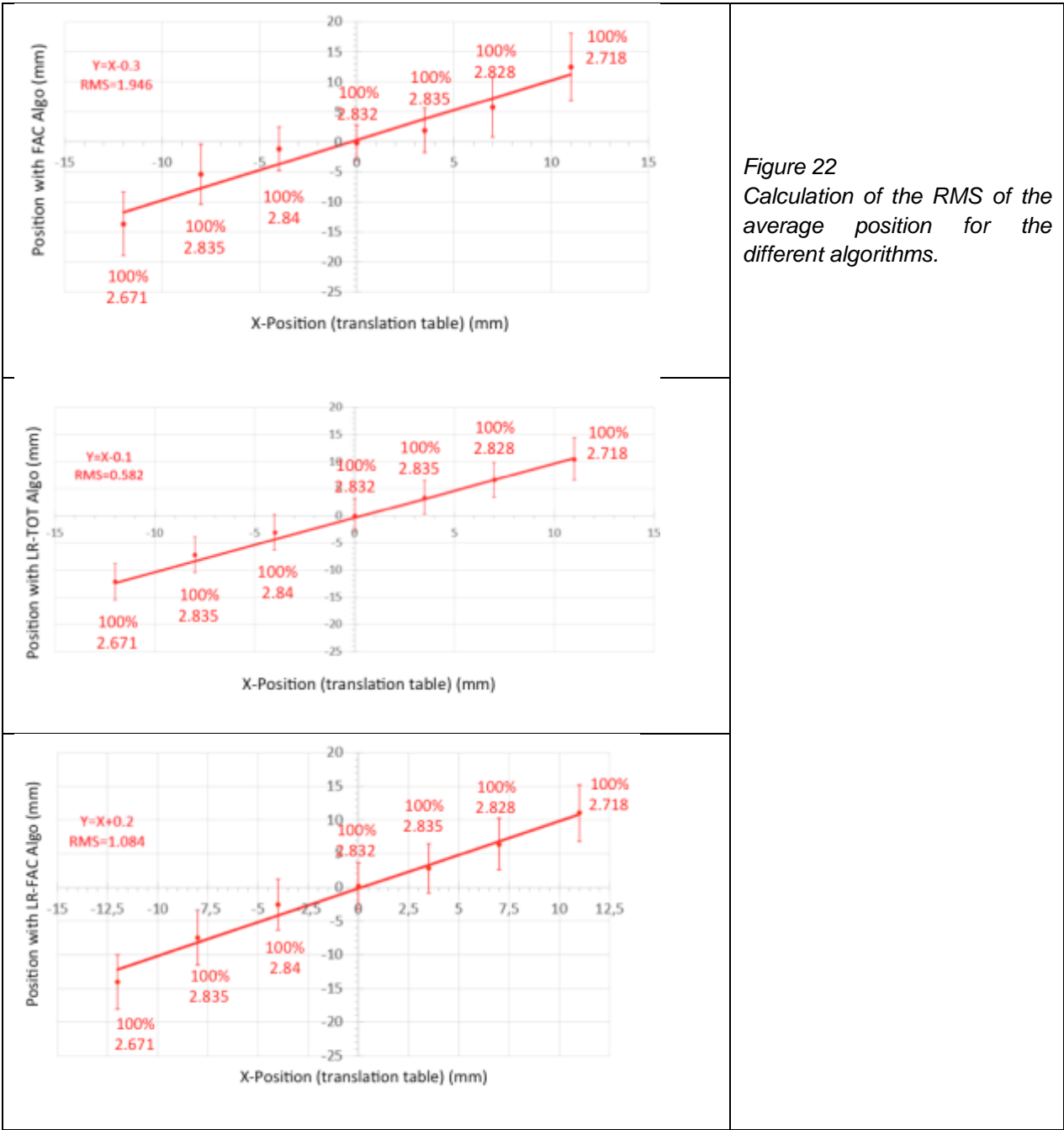


Figure 22
Calculation of the RMS of the average position for the different algorithms.

8 Conclusion

The RAMSES detector is in fabrication with a new grid design, optimized for detection efficiency, spatial uniformity, and low background.



We made the choice of a modular and light mechanics compatible with operation in vacuum. One consequence is that it requires operating the detector at low gas pressure. Until a dedicated gas vessel is built for the RAMSES MultiGrid detector, we have adapted and used two already existing MultiGrid detector vessels to study more in detail the performance of this technique at low gas pressure.

One measurement shows that a pressure around 200 mbar allows minimizing the charge collection. The average dead time (or TOT) measured at this pressure after optimization of the shaping amplifier is 320 ns, a factor of 10 better than what was measured during the CRISP project at atmospheric pressure and non optimized amplifiers.

We demonstrated that the detector efficiency is constant from 1 bar to 50 mbar, and that the plateau ranges are very similar from 50 mbar to 200 mbar, which makes the detector non sensitive to small variations of the pressure.

Important is the choice of the materials for internal components: although the detector supports easily outgassing materials, they should be minimized in quantity in order to minimize the gas flow. The effect of the outgasing is directly proportional to the inverse of the detection gas pressure, we need to multiply the gas flow by 10 if the pressure is reduced by 10.

In view of improving the localization precision, we recorded digitized signals on neighboring grids for different beam positions in order to test several localization algorithms. Preliminary results show that, among the algorithms tested, the one based on the comparison of the neighboring Time-Over-Threshold signals is the most efficient. A gain of 3 has been achieved compared to the standard First Active Channel algorithm. The so-called Left-Right TOT algorithm could be very easily implemented in the acquisition system without modification of the hardware.

We demonstrated that the MG detector can sustain very high counting rate without difficulties, and we couldn't see evidence of ageing after 15 hours of intense irradiation.

The crosstalk due to capacitive coupling between the grids has been measured: 16% for the individual grids of MG12, and 30% for the grids of RAMSES. We realized only very recently that this high values of the crosstalk is due to the high entrance impedance of the readout electronics; it has been strongly reduced with a minor change of the electronics.

One column of the RAMSES grids has been mounted besides 3 columns of CRISP grids in the RAMSES prototype to perform comparisons between the 2 designs. Preliminary measurements with this setup confirm the good performances with the new design.

For the near future, the newly developed gas control system will be tested in the vacuum chamber, and a new campaign of measurement on a neutron beam line will start after the ILL reactor restart in October 2017.

9 Bibliography

- [1] A. Khaplanov et al., Multi-Grid Boron-10 detector for large area applications in neutron scattering science, arXiv:1209.0566 (2012)
- [2] J. Correa et al., 10B4C Multi-Grid as an Alternative to 3He for Large Area Neutron Detectors, Trans. Nucl. Sc. (2013) DOI: 10.1109/TNS.2012.2227798
- [3] J. Correa 10B4C Multi-Grid as an Alternative to 3He for Large Area Neutron Detectors PhD thesis, ILL and Uni Zaragoza (2012)
- [4] B. Guerard et al., 10B multi-grid proportional gas counters for large area thermal neutron detectors, Nucl. Instr. Meth. A (2012) <http://dx.doi.org/10.1016/j.nima.2012.12.021>
- [5] J Birch et al., In-beam test of the Boron-10 Multi-Grid neutron detector at the IN6 time-offlight



spectrometer at the ILL J. Phys.: Conf. Ser. (2014) 528 012040 doi:10.1088/1742-6596/528/1/012040

[6] C. Höglund, et al., B₄C thin films for neutron detection, J. Appl. Phys. 111(104908) (2012)

[7] A. Khaplanov et al., Investigation of gamma-ray sensitivity of neutron detectors based on thin converter films J. Inst. (2013) 1748-0221 8 P10025 doi:10.1088/1748-0221/8/10/P10025

[8] A. Khaplanov et al., Investigation of background in large-area neutron detectors due to alpha emission from impurities in aluminium J. Inst. (2015) 10 P10019 doi:10.1088/1748-0221/10/10/P10019



Annex 1: The gas delivery system

In parallel to the detector development, an automated gas delivery system is currently studied to operate the detector in safe conditions. In this report, we draw the main characteristics of the system.

Description of the system

A first scheme of the gas delivery system is given in Figure 1 and all the components are listed below:

List of components:

- TOF Chamber: $V = 1000$ L
- Detector: $V = 250$ L, Leakage rate = 3.75 mb.L/min @ 50 mbar (Virtual valve **Leak**), Manual inlet and outlet valves V_{d_in} and V_{d_out} , internal Pressure gauge **PG_{d1}**
- Manual vacuum valve **V_c**
- Main pump **P_m** + N.C. electro-valve **EV_{pm}**
- Secondary pump **P_s** + N.C. electro-valve **EV_{ps}**
- Dry Air bottle + manual pressure regulator + N.C. electro-valve **EV_a**.
- Gas mix bottle + manual pressure regulator + N.C. electro-valve **EV_g**.
- Differential Pressure Gauge **DPG**
- High flowrate (>25L/min) Safety electro-valve N.O. **EV_s**
- Dual Valve Pressure Controller for the TOF chamber **DVPC_c** with an internal pressure gauge.
- Single Valve Pressure Controller for the detector **SVPC_d**, coupled to a pressure gauge **PG_{d1}**.
- High flowrate (> 25L/min) bypass electro-valve N.O. **EV_d**
- Low (~50 mL/min) and High (~25L/min) volumetric flow rate Flowmeter for gas injection **F_{i_LF}** and **F_{i_HF}**
- Low flow (~50 mL/min) Flow Controller for detector outlet **FC_{o_LF}**
- High flow (0-100 L/min) electro-valve for detector outlet **EV_{o_HF}**
- Humidity sensor **H**
- Temperature Sensor **T°**
- Electronic Switches on/off for Low and High Voltage supplies **LV** and **HV**
- A drying system for the air inside the chamber

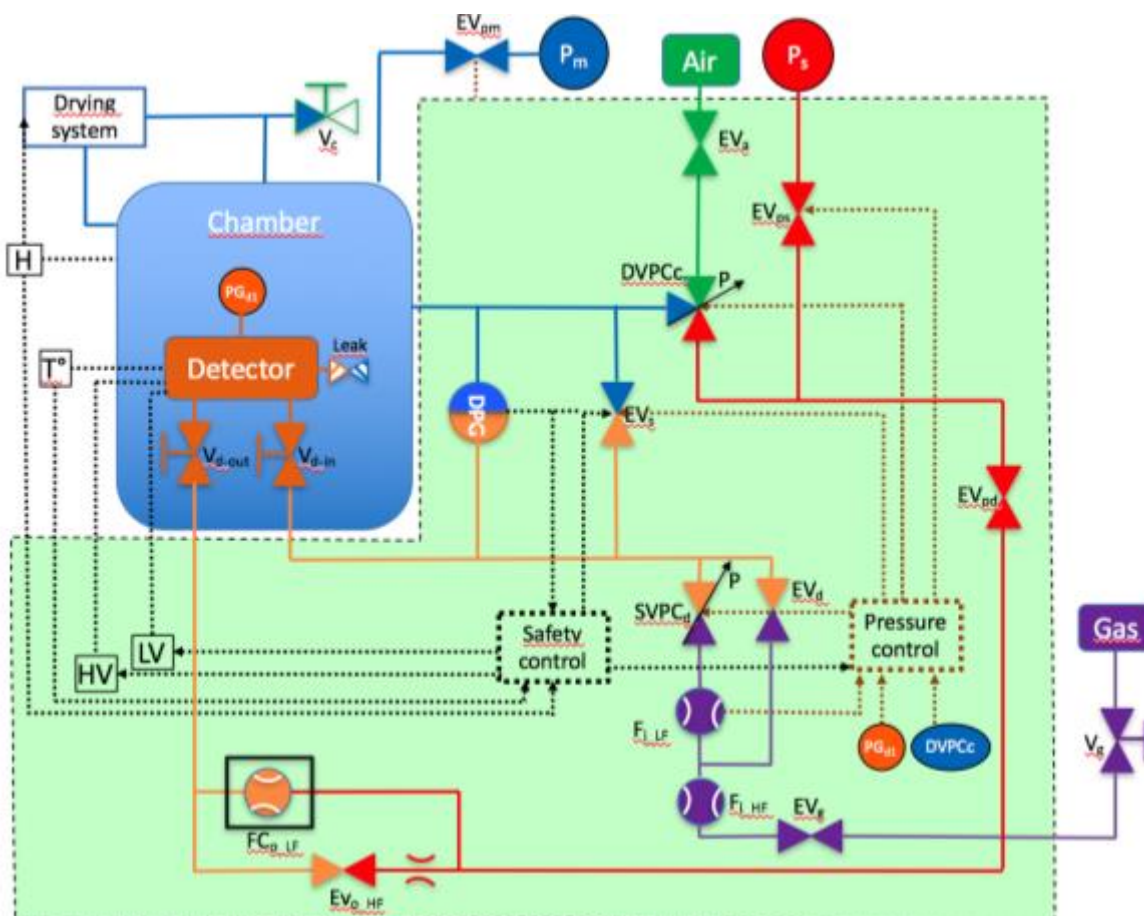


Figure 1: Scheme of the gas delivery system

The detector is located in the TOF chamber. At any time, the extreme limit of differential pressure between the two volumes is fixed at 50 mbar. If for any reason, the value, which is permanently monitored with a differential pressure gauge **DPG**, exceeds the limit, the safety electro-valve **EV_s** is automatically open and the detector is shut down. In case of electrical failure, this valve is Normally Open (N.O.).

To regulate the pressure inside the TOF chamber that constitutes a closed volume with possible gas entrance (detector leak or TOF chamber leak), the system is provided with a dual valve pressure controller **DVPCc**. The supply is connected to fresh air and the exhaust to the regulation pumping station **P_s**. To regulate the pressure inside the detector, the system is equipped with a single valve pressure controller **SVPCd** connected to the gas mix supply. The flow of gas is monitored thanks to two flowmeters **F_{L_LF}** and **F_{L_HF}**, each of them being dedicated for different ranges of flowrate. As the pressure controller is dimensioned for low flowrate, a by-pass electro-valve **EV_d** has been foreseen to allow purging the pipes more efficiently and doing high flowrate flushing. The gas mix inside the detector needs to be flushed permanently at low flowrate (<50 mL/min) and low pressure (50-100 mbar) due to outgassing components. This is made through the leak of the detector plus the flow controller **FC_{o_LF}** which can control precisely the desired flushing rate. The detector leak is measured by the difference



between the 2 flowmeters; in and out. Since it is always tricky to play with both flowrate controller and pressure controller at the same time, the flowrate controller should be open only when the pressure has been stabilized inside the detector.

The detector can also be used at atmospheric pressure for beamline tests. In that case, the filling of the detector is made by high volume flushing of gas mix to wipe the air out of the detector. This procedure can be made manually playing with the pressure regulator of the gas bottle, and the opening of the high-flowrate electro-valve [EV_{o_HF}](#).

Depending on the gas the chamber is filled in with (probably air), it may require a drying system to reduce neutron scattering except if the chamber is under vacuum. This system could also cool the gas down and consequently decrease the temperature of the electronics.

We planned to drive this regulation system with an automat that allows the user to launch automatic sequences but also semi-automatic and manual processes. The main feature of the automat is to make any kind of intervention (automatic, semi-automatic or manual) safe so that the detector cannot be damaged.

Annex2: Feedback on prototype mounting

Assembly of the RAMSES grids

The new design is based on columns of 16 20-mm-thick grids with 0.5 mm space in between. Each grid is made of 18 radial blades (7 of them are doubled) and 25 transversal blades which constitutes an assembly of 576 cells. The angular acceptance of the detector is about 6.1° for 2.5 m curvature radius. The blades are either in aluminum alloy (Al1050A) or in low alpha-emitting aluminum (almost pure) coated with 900 nm-thick ^{10}B . Every blade is provided with a corresponding number of notches which can welcome the crossing blades.



The mounting of the grids follow a proper checklist. First the blades have to be separated from their holding part with a cutting plier. The small pinching at the cut edge can be removed with a box cutter. Then all the outer blades are placed into the unibody aluminum frame against the outer walls. Next, all radial blades are inserted. Finally, the transversal blades are embedded into the dedicated notches. When all the blades are in position, they are welded at both ends to the frame with a millisecond TIG welding machine.

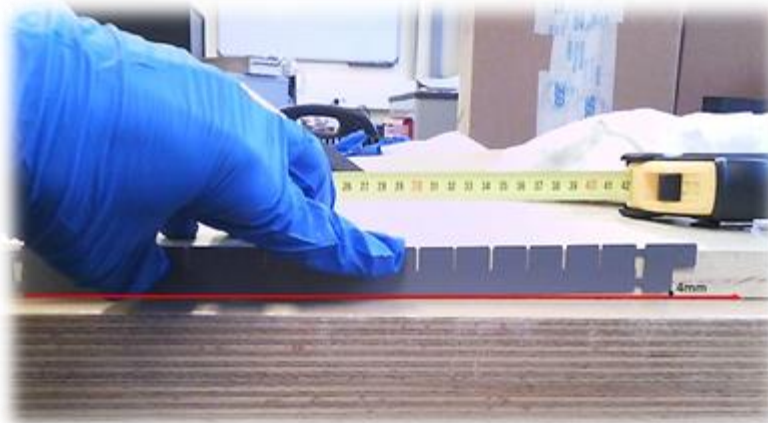
This scheme of mounting works pretty well for the blades made of Al1050. Nevertheless, the blades in pure aluminum cannot be inserted as easily as the Al1050 ones. Indeed, during the coating process, the blades are heated at a temperature about 300°C and they stretch out according to their thermal expansion coefficient. Once cooled down, it appears that the pure aluminum blades are longer than their initial state so that they cannot be inserted into the frame anymore. It could come from the fact that the ^{10}B coating prevent the blade from retracting as much as it expanded (too big difference of thermal expansion coefficients) but regarding the small thickness of the coating it seems unlikely. This



problem is nonetheless not seen for Al1050 blades. The explanation not to see this effect on both material could arise from the fact that the limit of elasticity is exceeded only for the first material which implies a permanent deformation even after the temperature has decreased. Consequently, the interval between two blades is slightly modified. To be inserted into the frame one has to remove a small amount of material at both ends. This operation is particularly time consuming and tricky because one still need to respect symmetry with manual cutting. For the next detector, it is clear that this problem should be corrected or at least the frame must be adapted to be able to accept the stretched blades.

For the same presumed reasons as those mentioned before, it exists another problem for the pure aluminum blades, mostly for the long ones. As a result of the coating process under quite high temperature conditions, the long blades are curved perpendicularly from their long edge and along the plane of the blade. The concavity from 3 to 4 millimeters is always on the side of the notches which is in agreement with the constrains in the material during the heating process. Since the grids are separated with of a gap of only 0.5 mm, such a deformation of the transversal blades is obviously an issue. Currently, we have to correct this defect manually because the resulting problem is shortcuts between the grids. For the future, it would be much better to suppress it. Two leads are investigated to reduce the bending: The first one consists in reducing the height of the notches which still implies a deformation but a smaller one.

The second option comes from alternating the position of the notches from one side to the other. In this extent, it seems that the bending effect from one side can counterbalance the one from the other side.



Some basic simulations have been done with Solidworks® simulation package to study more deeply these distortions. It

consists in observing the constraints and the deformed shape of a 25-cm-long almost pure aluminum blade after a heating process from 20 to 300 °C. As expected, several areas of the blade have constraints higher than the elasticity limit which prevent the blade from getting back to its initial state when temperature decrease.



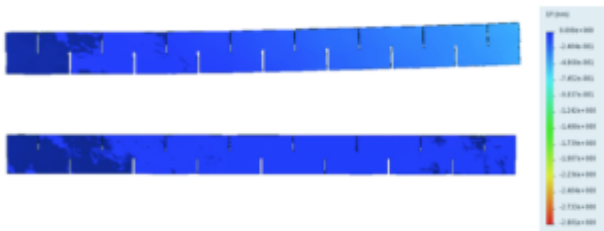
If you look at the deformation along the orthogonal axis, that means at the bending effect, simulations give values about 3.0 mm in agreement with the observations. (Deformations on the picture are not at scale).



We previously mentioned two options to counter this effect that have been also simulated. Thus, the reduction of the height of the slits by half reduce the bending effect by a factor of a third (1.8 mm) as we can see on the next plot.



If we now alternate the notches, the bending effect a further diminished with a maximal deformation along orthogonal axis of 0.49 mm (The color scale is still the same). This time the concavity is on the opposite side because there is one more slit on this side. Finally, if we combined a reduction by one fourth of the height of the slits to the alternating of their position, the maximal bending effect calculated is lower than 0.1 mm (The color scale is still the same). This solution can definitely be studied for the future prototype detector for which we foresee to have a double-sized grid.



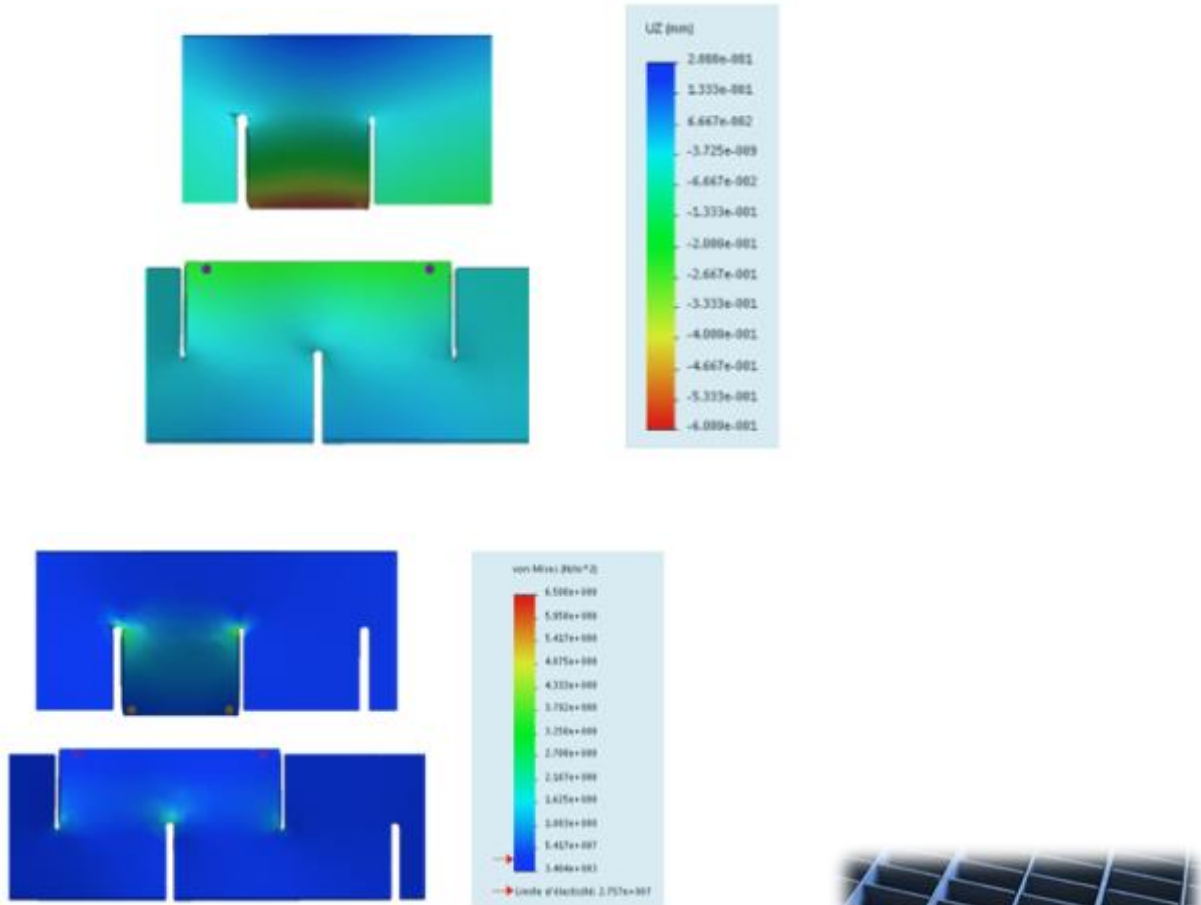
The simulations give another interesting result that confirms the observations about the strain of the blades along the blade axis ranging from 0.6 to 0.7 mm. On a 25-cm long blade the calculations give a strain of 0.7 mm at the end of the blade. The configuration mentioned before with alternate slits is also interesting in reducing a bit the total lengthening down to 0.52 mm.



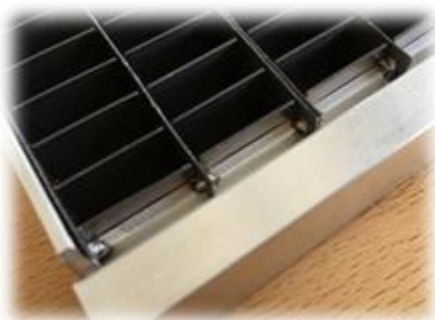
Another comparison can be made regarding the stiffness of a tooth for both configuration. Thus, applying to the edge of the tooth a force of 10 N, we can study the induced displacement and the



mechanical constraints. The results (next graphs) are in favor of the alternate slits blade since constraints and displacements are lower – divided by approximately a factor 2. This mechanical aspect is rather important for the grid mounting procedure since it contributes to the misalignment of the cells from one grid the next one. If the teeth are stiffer, then the accidental deformations occurring during the insertion and arrangement of the blades should be reduced.



The final step of the grid assembling is the welding on the blades onto the frame. This operation is easy for the radial blades that are provided with an attach external to the frame. For the transverse ones, this is a bit more complicated since the welding must be made at the intersection of the crossing blades. There are two main drawbacks: the





“teeth” of the blades have a rounded corner so the intersection is not really well defined and there is a lack of matter. The resulting weld is a small “crater”. Moreover, the small projections of aluminum during the welding pulse are likely to hold on to the cells walls, increasing the contamination of the cells but also the probability of breakdowns during operation at high voltages. A sort of mask could be used to prevent from that projections to enter the cells but the small space available makes difficult the handling. An idea to suppress these welding points would be to sandwich transversal blades between two radial blades; It means that the notches of the long blades should be alternate exactly as it has been presented previously. Here, we can see the double benefit from implementing the kind of configuration. The frame should be adapted to make the insertion of radial blades to the other side possible and the blades could be weld the same way as before.

At the end of the assembling process, we would like to control that the blades are correctly assembled. Considering the number of cells, a standard metrology measurement would be too long to put in place. As the precision required is not so high, about 0.5 mm, (anyway we could hardly ask for more regarding the malleability of such aluminum), we have imagined an optical way to control that the blades are in the right place. We built a mask with black-ink on a plastic transparent foil that constitutes the negative profile of the final grid. With a backlighting under the mask and putting the grid aligned with the mask, we are able to see directly if one blade or more is bent. This solution is quite convenient in the extent that we can correct directly the defects.



Assembly of the RAMSES prototype

For preliminary tests, only half of the charge division networks (and corresponding number of wires) were mounted on the detector. Each group of 4 wires was connected to the next one through either 75 or 200 Ohms resistors. Since then, based upon our last results, we have decided to implement only 200 Ohms resistors. The



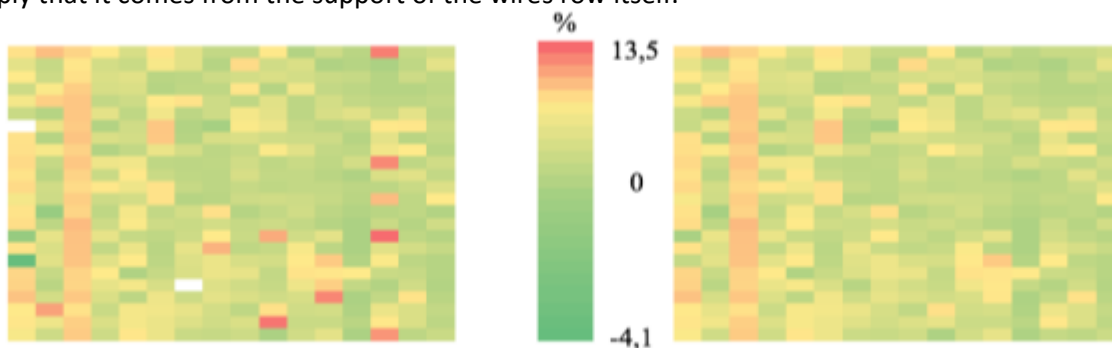
The two sets of grids mounted next to each other on the RAMSES prototype frame



remaining wires have thus been welded. Because the number of channels available with RAMSES prototype allows it, we decided to have half of the detector with two 5 kΩ networks made of 24 groups of 4 wires, and the second half composed of four 5 kΩ networks made of 24 groups of 2 wires. The latter is very similar in terms of cells' dimensions to the former grids. With this configuration, we should be able to have a nice comparison between the two types of grids during a beam time.

Before closing the detector, each wire has been visually and “electrically” checked so that no shortcut between cathodes or wires, or missing connection can be found. The resistance of each wire has also been measured and used to localize possible welding issues. The typical resistance for a ~35-cm-long-20μm “free” wire is approximately 97,5 Ω. Our wires are stretched out with a 0,06 N force. The resistance should remain the same since the distance is not modified between two welding pads. Nevertheless, in some cases, the resistance value can be slightly higher when the wires have some defects or when there is a slight misalignment (wire not well centered on the pad and a resulting welding at the “end of the pad”).

Below there is a map of every resistance value before and after wire replacements operated when resistance value was 5 % higher than the mean value. Replacements operated show that there obviously were some defects (on wire or welding) since the new value is much closer from the mean one. Still remains one row of wires that exhibits higher values. This is not explained yet since replacements of some wires did not change anything. Besides, the whole row is concerned, which may imply that it comes from the support of the wires row itself.



Left : Map of deviation (in %) from the mean resistance value (97,72 Ω) before replacing wires.

Right : Map of deviation (in %) from the mean resistance value (97,46 Ω) after replacing wires.